High-order solutions of transitional flow over the SD7003 airfoil using compact finite-differencing and filtering

Daniel J. Garmann and Miguel R. Visbal
Air Force Research Laboratory, Wright-Patterson AFB, OH 45433

Code Description

All simulations are performed with the extensively validated high-order, Navier-Stokes solver, FDL3DI[1;2]. In this code, a finite-difference approach is employed to discretize the full, compressible Navier-Stokes equations. All spatial derivatives are obtained with high-order compact-differencing schemes.[3] At boundary points, higher-order one sided formulas are utilized which retain the tridiagonal form of the scheme[1;2]. Typically, Neumann boundary conditions are implemented with third-order, one-sided expressions. The derivatives of the inviscid fluxes are obtained by forming the fluxes at the nodes and differentiating each component with the compact differencing scheme. Viscous terms are obtained by first computing the derivatives of the primitive variables. The components of the viscous fluxes are then constructed at each node and differentiated by a second application of the same scheme.

In order to eliminate spurious components of the solution, a high-order, low-pass spatial filtering technique[1;4] is incorporated which is based on templates proposed in References 3 and 5. With proper choice of coefficients, it provides a $2N^{th}$-order formula on a $2N+1$ point stencil. These coefficients, along with representative filter transfer functions, can be found in References[2] and[4]. The filter is applied to the conserved variables along each transformed coordinate direction once after each time step or sub-iteration. For the near-boundary points, the filtering strategies described in References[1] and[4] are used. For transitional and turbulent flows, the previous high-fidelity spatial algorithmic components provide an effective implicit LES approach in lieu of traditional SGS models, as demonstrated in References 6 and 7. All computations presented here are performed with a sixth-order interior discretization scheme coupled with an eighth-order accurate implicit filter.

Time marching of the governing equations is achieved through the iterative, implicit approximately-factored integration method of Beam and Warming[8]. This method has been simplified through the diagonalization of Pulliam and Chaussee[9] and supplemented with the use of Newton-like sub-iterations to achieve second-order accuracy[6;7]. Sub-iterations are commonly used to reduce errors due to factorization, linearization, diagonalization, and explicit specification of boundary conditions[10]. Fourth-order, nonlinear dissipation terms[11;12] are also appended to the implicit operator in order to augment stability.

Case Summary

The case being analyzed corresponds to "C3.3: Transitional Flow over a SD7003 Wing, Case 2" as described by the high-order workshop committee. The airfoil corresponds to the Selig SD7003 airfoil, which is shown in Fig. 1. The maximum thickness is 8.5% with a maximum camber of

1.45% at the 35% chord location. The sharp trailing edge has been rounded with a circular arc with a radius, $r/c \approx 0.0004$, in order to facilitate the use of an O-grid topology. The planar airfoil geometry is extended 0.2 chords in the spanwise direction to produce a wing section.

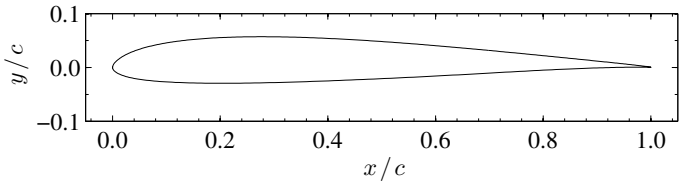

Figure 1: SD7003 airfoil geometry

Simulations are carried out with a free-stream Mach number, $M_\infty = 0.1$, and chord-based Reynolds number, $\mathrm{Re_c} = 60,000$. The angle of attack, α, is prescribed as 8°. The time-mean flow at these conditions is characterized by a short laminar separation bubble originating from around the 2% chord location and reattaching around the 26% chord location.

A time-step of 0.0001 convective times is used for all simulations. Each solution is also initialized from a uniform stream and run for 20-30 convective times to eliminate any spurious transient data. Statistical information on velocity and pressure across the span at 10 chordwise positions is then gathered for the next 10 convective times. This data is used to compute spatial and temporal energy spectra and mean flow field data.

The fine mesh solution, discussed below is computed in parallel on 208 processors resulting in an average time of 1.329 seconds per iteration. With 300,000-400,000 iterations needed, this equates to 111-148 hours of total run time per simulation.

Computational Mesh and Boundary Conditions

The computational domain around the SD7003 airfoil is discretized using an O-grid, structured mesh topology. The baseline, fine mesh is prescribed with 516 gridlines circumferentially around the airfoil surface (ξ-direction) with clustering at the leading and trailing edges and 66% of the points distributed on the upper surface in order to maintain sufficient resolution in the near-body wake region at positive angles of attack. In the normal (η) direction, 304 points are projected outward to nearly 100 chords from the surface to a circular, farfield boundary. The planar, O-grid is uniformly extruded in the spanwise (ζ) direction across an extent of 0.2 chords using 80 points.

In order to investigate grid dependance, the baseline computational mesh is coarsened in the ξ-direction aft of the quarter chord position on the upper surface. Coarsening in this region alone is in an effort to modify the spatial resolution only in the regions of the smallest scales while reducing the effect on the potential flow around the airfoil. Two meshes were generated that reduced the number of ξ-gridlines in this region by 50% and 75%, respectively, while maintaining the leading and trailing edge spacing of the fine grid. A depiction of the three meshes is shown in Fig. 2, where only every third gridline in the ξ- and η-directions is present for clarity. Details of the point distributions are documented in Table 1.

The boundary conditions are prescribed as follows. Along the airfoil surface, a no-slip, adiabatic condition is employed in conjunction with a fourth-order, extrapolated zero normal pressure gradient. Along the far field boundary, located more than 100 chord lengths away from the airfoil, free-stream conditions are specified. It should be noted that near this boundary, the meshes are stretched rapidly, which in conjunction with the low-pass spatial filter provides a buffer-type treatment found previously[15] to be quite effective in reducing spurious reflections. Along the branch cut

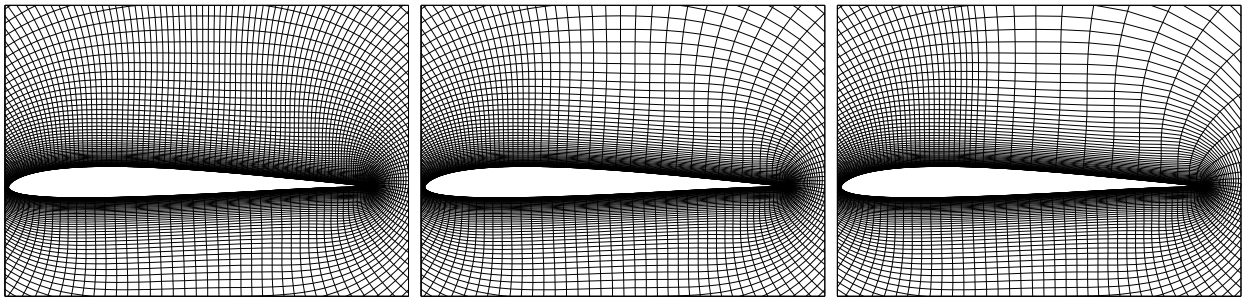

(a) Fine (b) Medium (c) Coarse

Figure 2: Resolution comparison of fine, medium, and coarse meshes

of the O-grid topology and on the spanwise boundaries, spatial periodicity is imposed by means of a five-point grid overlap to maintain the stencil of the high-order discretization and filtering schemes.

Table 1: Computational Mesh Dimensions and Spacing

Mesh	Dimensions	N_U	$(\Delta s/c)_{\max}$	$(\Delta s/c)_{\text{LE}}$	$(\Delta s/c)_{\text{TE}}$	$(\Delta n/c)_i$
Fine	516 x 304 x 80	343	0.0051	0.001	0.0001	0.00003
Medium	402 x 304 x 80	229	0.0141	-	-	-
Coarse	373 x 304 x 80	200	0.0259	-	-	-

N_U	number of points on upper surface
$(\Delta s/c)_{\max}$	maximum surface spacing on upper surface
$(\Delta s/c)_{\text{LE}}$, $(\Delta s/c)_{\text{TE}}$	leading and trailing edge surface spacing
$(\Delta n/c)_i$	initial wall normal spacing

Results

As mentioned in the case description, at an incidence of 8° the time-mean flow about the SD7003 airfoil is characterized by a short separation bubble, where separation occurs almost immediately around the 2% chord location and reattaches just past the quarter chord position. This can be seen in the time-mean and span-averaged flowfield contours of Fig. 3. Consequently, a long region and high degree of turbulence is present on the aft portion of the upper surface of the wing section as depicted by the instantaneous Q-criterion iso-surfaces of Fig. 4 from the fine grid solution.

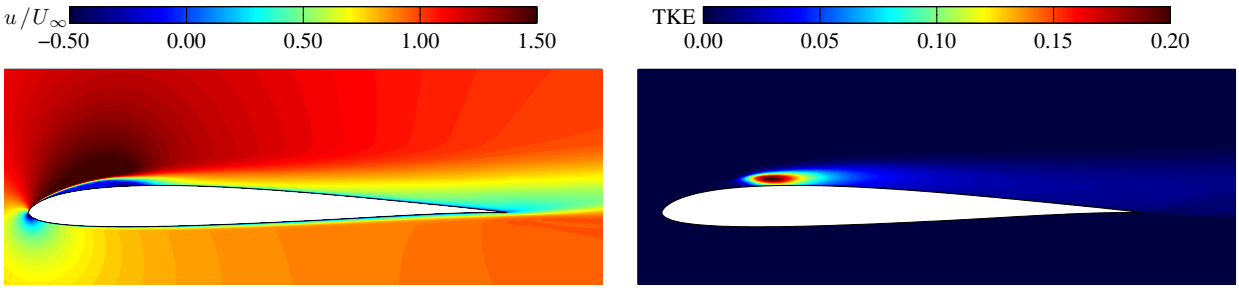

(a) u-velocity (b) TKE

Figure 3: Time-mean solution showing (a) u-velocity and (b) turbulent kinetic energy for $\alpha = 8°$

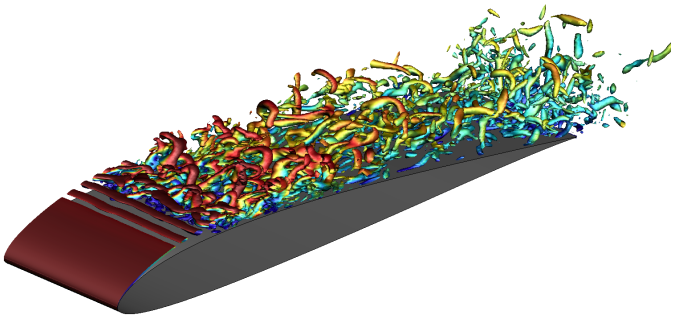

Figure 4: Instantaneous flowfield structure showing Q-criterion iso-surfaces of 500 for $\alpha = 8°$

The spatial filtering technique employed in the ILES allows for a free-constant, $0.3 \leq \alpha_f < 0.5$, to control the degree of filtering. Lower values lead to more dissipation, while values approaching 0.5 reduce the amount of filtering as seen by the filter transfer function in Fig. 5. In order to ensure that the filter is not overly dissipative for the current study, several coefficients are examined corresponding to $\alpha_f = 0.4$, 0.45, and 0.475 on the fine mesh.

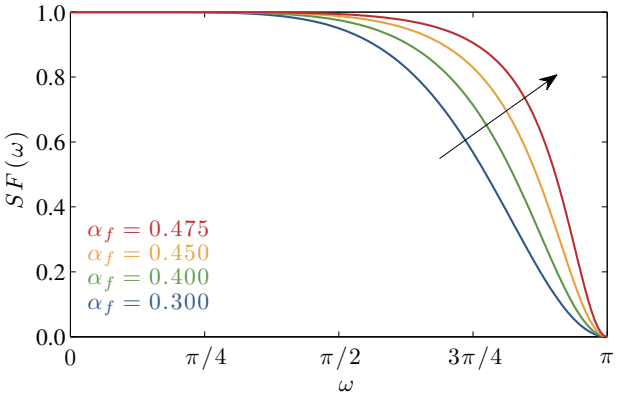

Figure 5: Implicit filter transfer function for $\alpha_f = 0.3$, 0.4, 0.45, and 0.475

Profiles of the streamwise velocity and mean-squared fluctuations of u as well as surface distributions of the pressure and skin friction from the time-mean solution employing each coefficient are displayed in Fig. 6. The profiles are taken normal to the surface every 10% chord, except for the first profile which is taken at 2.5% chord. The low-dissipation filter coefficients all produce similar profiles and distributions, indicating that the dominant scales associated with this flow and mesh resolution are being captured by using a filter coefficient of 0.4. This claim is further substantiated when analyzing the spatial and temporal frequency spectra at various chordwise locations for each of the solutions, which are also depicted in Fig. 6. Both spectra show practically identical content across the band of frequencies. A slightly wider band of wave numbers is present for the higher filter coefficients, but with such little energy, these modes do not affect the time-mean solution. Based on these results, the filter coefficient of 0.4 is used for the remainder of this study.

In order to examine the mesh dependence on this flow, the afore-mentioned grid resolutions are all simulated. A measure of the resolution in wall units for each mesh is given in Table 2 for the streamwise (Δs^+), normal (Δn^+), and spanwise (Δz^+) directions. The tabulated values show the maximum of each component taken only in the region of turbulence on the aft portion of the upper surface of the airfoil. The fine mesh gives two and three times more resolution than the medium and

coarse meshes, respectively, in the streamwise direction. The Δn^+ values at the surface increase slightly with more resolution but are well under unity. Decreased resolution also promotes lower values of Δz^+, but with minimal change from the baseline, fine mesh.

Table 2: Maximum grid spacing in wall units

Mesh	Δs^+	Δn^+	Δz^+
Fine	20.6	0.137	10.9
Medium	41.9	0.129	10.4
Coarse	62.0	0.122	9.78

The time-mean solution from each of the meshes is depicted in Fig. 7 through profiles of streamwise velocity and mean-squared fluctuations of u as well as distributions of skin friction and pressure coefficient on the surface of the airfoil. Each plot plot shows a convergence with increased spatial resolution. This is also seen in the tabulated chordwise positions of separation and aft-most reattachment in Table 3. These values show a shorter laminar separation bubble with increased resolution. The spatial and temporal frequency spectra also shown in Fig. 7 reveal a significant change in the content of the flow only past transition, where lower resolution reduces the band of frequencies while increasing the energy in the lowest modes. Additionally, the mean lift, drag, and moment coefficients are tabulated in Table 4, where the lift is around 0.97, the drag is approximately 0.04, and the moment is about -0.02 for all meshes. These results give confidence in the fine mesh solution for proper resolution of the dominant features of the flow at these conditions.

Table 3: Chordwise positions of separation and reattachment

Mesh	x_1/c	x_2/c
Fine	0.023	0.259
Medium	0.022	0.267
Coarse	0.023	0.284

x_1/c separation point
x_2/c aft-most reattachment point

Table 4: Mean aerodynamic loads

Mesh	$\overline{C_L}$	$\overline{C_D}$	$\overline{C_{M,c/4}}$
Fine	0.9696	0.0391	-0.0197
Medium	0.9838	0.0418	-0.0237
Coarse	0.9703	0.0441	-0.0255

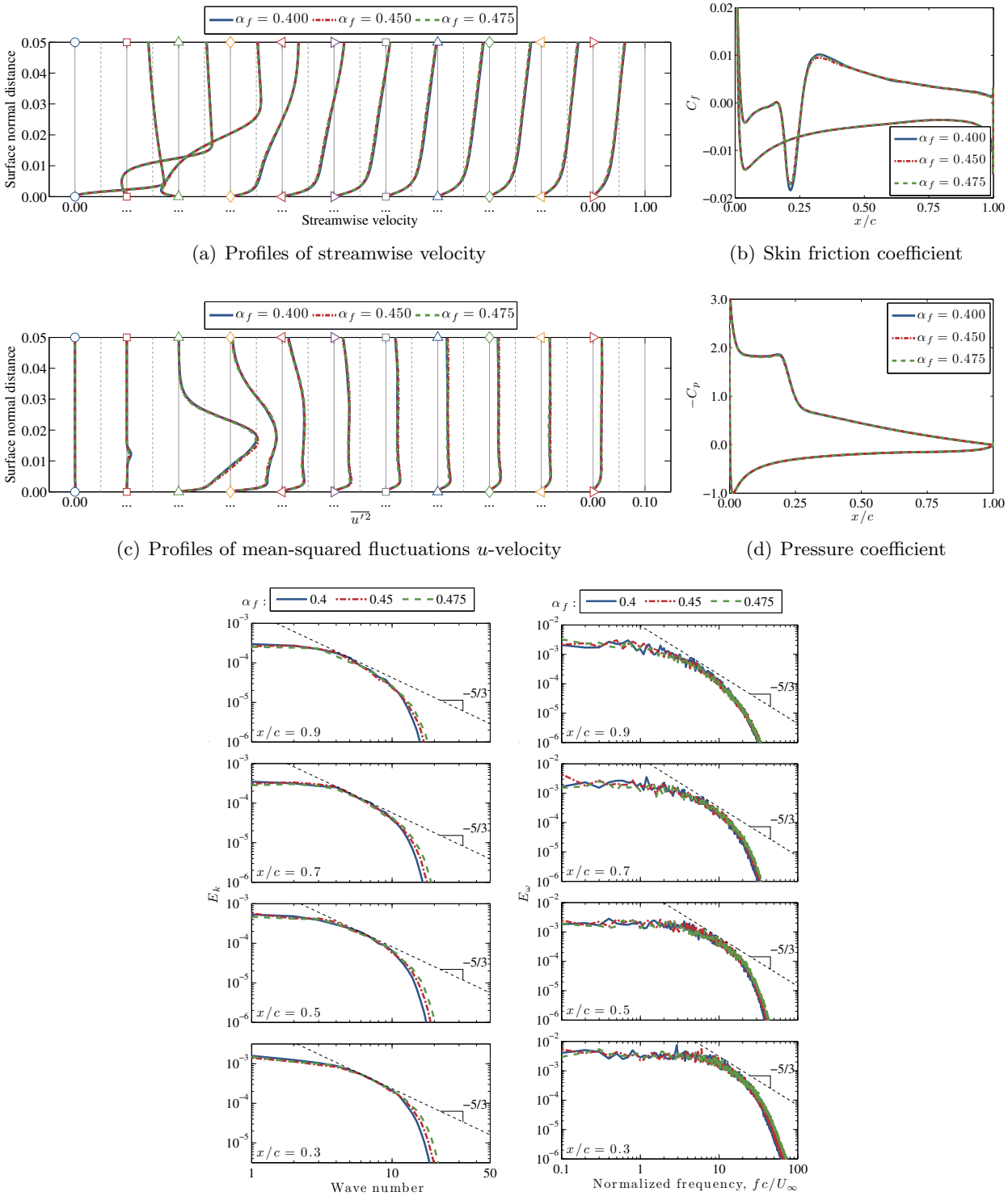

(a) Profiles of streamwise velocity

(b) Skin friction coefficient

(c) Profiles of mean-squared fluctuations u-velocity

(d) Pressure coefficient

(e) Spatial energy spectra, $E(k)$

(f) Temporal energy spectra, $E(\omega)$

Figure 6: Comparisons of time-mean flow field and spatial and temporal energy spectra at various chord-wise locations computed from the ILES solutions with filter coefficients of 0.400, 0.450, and 0.475 on the fine mesh

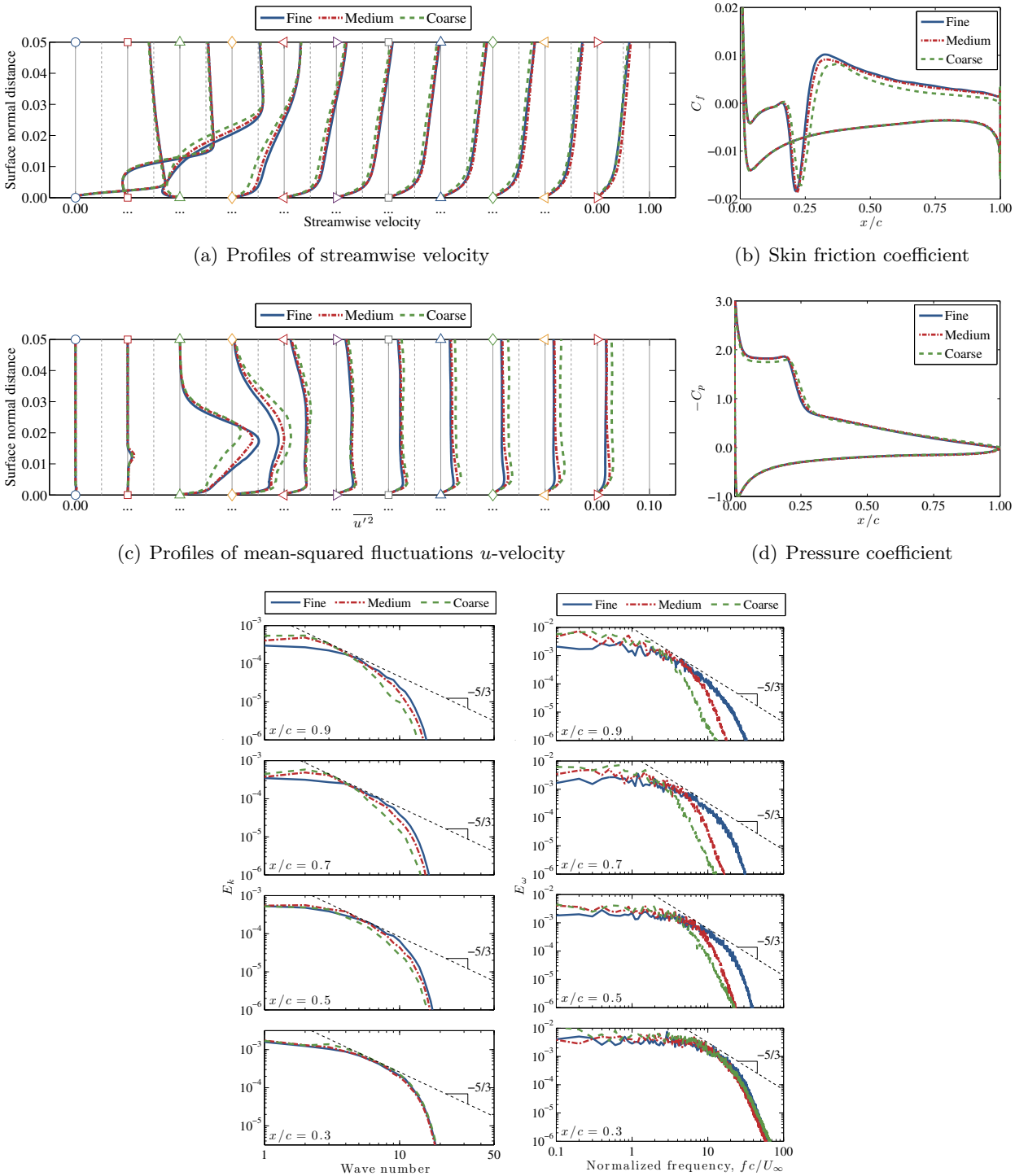

(a) Profiles of streamwise velocity

(b) Skin friction coefficient

(c) Profiles of mean-squared fluctuations u-velocity

(d) Pressure coefficient

(e) Spatial energy spectra, E_k

(f) Temporal energy spectra, E_ω

Figure 7: Comparisons of time-mean flowfield and spatial and temporal energy spectra at various chord-wise locations computed from the fine, medium, and coarse mesh solutions

References

[1] M.R. Visbal and D.V. Gaitonde. High-order accurate methods for complex unsteady subsonic flows. *AIAA Journal*, 37(10):1231–1239, 1999.

[2] D.V. Gaitonde and M.R. Visbal. High-order schemes for navier-stokes equations: Algorithm and implementation into fdl3di. Technical Report AFRL-VA-WP-TR-1998-3060, Air Force Research Laboratory, Wright-Patterson AFB, 1998.

[3] S.K. Lele. Compact finite difference schemes with spectral-like resolution. *Journal of Computational Physics*, 103:16–42, 1992.

[4] D.V. Gaitonde and M.R. Visbal. Further development of a navier-stokes solution procedure based on higher-order formulas. AIAA Paper 99-0557, AIAA, 1999.

[5] P. Alpert. Implicit filtering in conjunction with explicit filtering. *Journal of Computational Physics*, 44:212–219, 1981.

[6] M.R. Visbal and D.P. Rizzetta. Large-eddy simulation on curvilinear grids using compact differencing and filtering schemes. *Journal of Fluids Engineering*, 124:836–847, 2002.

[7] M.R. Visbal, P.E. Morgan, and D.P. Rizzetta. An implicit les approach based on high-order compact differencing and filtering schemes. AIAA Paper 2003-4098, AIAA, June 2003.

[8] R. Beam and R. Warming. An implicit factored scheme for the compressible navier-stokes equations. *AIAA Journal*, 16(4):393–402, 1978.

[9] T.H. Pulliam and D.S. Chaussee. A diagonal form of an implicit approximate-factorization algorithm. *Journal of Computational Physics*, 17(10):347–363, 1981.

[10] D.P. Rizzetta, M.R. Visbal, and P.E. Morgan. A high-order compact finite-difference scheme for large-eddy simulation of active flow control (invited). AIAA Paper 2008-526, AIAA, 2008.

[11] A. Jameson, W. Schmidt, and E. Turkel. Numerical solutions of the euler equations by finite volume methods using runge-kutta time stepping schemes. AIAA Paper 1981-1259, AIAA, 1981.

[12] T.H. Pulliam. Artificial dissipation models for the euler equations. *AIAA Journal*, 24(12): 1931–1940, Dec. 1986.

[13] D.P. Rizzetta and M.R. Visbal. Numerical investigation of plasma-based control for low-reynolds number airfoil flows. AIAA Paper AIAA-2010-4255, AIAA, 2010.

[14] M.R. Visbal. High-fidelity simulations of transitional flow past a plunging airfoil. *AIAA Journal*, 47(11):2685–2697, 2009.

[15] M.R. Visbal and D. Gaitonde. Very high-order spatially implicit schemes for computational acoustics on curvilinear meshes. *Journal of Computational Acoustics*, 9(4):1259–1286, 2001.